

Spatial observation of Bose-Einstein condensation of ^{87}Rb in a confining potential

B. P. Anderson and M. A. Kasevich

Physics Department, Yale University, New Haven, Connecticut 06520

(Received 1 July 1998)

Bose-Einstein condensation of ^{87}Rb has been observed in a vapor cell time-averaged orbiting potential trap, and the trapped condensates have been studied using *in situ* absorption and dark-ground imaging methods. Condensates of 3×10^4 atoms were observed after 26 s of evaporative cooling. The evaporative cooling sequence consisted of a combination of cooling with ramping magnetic-field strengths and radio-frequency-induced cooling. The measured sizes, numbers of atoms, and transition temperatures of the condensates are consistent with theoretical predictions that include the effects of atomic interactions. [S1050-2947(99)50502-7]

PACS number(s): 03.75.Fi, 05.30.Jp, 32.80.Pj

The ground-breaking studies of Bose-Einstein condensed, dilute atomic vapors have enabled new tests of theory for weakly interacting degenerate Bose gases [1–3]. Important examples of such tests include measurements of condensate fraction and the mean-field interaction energy [4,5]. In previous experiments, these studies have been based on momentum distribution measurements that are extracted from images of initially condensed samples following an interval of free-space ballistic expansion. We present complementary measurements of these quantities based on analysis of direct images of ^{87}Rb condensates, made in a regime where the number of condensed atoms was small enough that the kinetic energy of the trapped atoms could not be ignored in comparison with the mean-field interaction energy.

Our experimental approach for condensate production paralleled that of the first JILA experiment [1]. Atoms were initially captured from a dilute Rb vapor into a magneto-optic trap (MOT) [6] operating in a modified dark-spot configuration [7,8]. Atoms were subsequently compressed [9] and cooled, optically pumped into the $F=2$, $m_f=2$ ground state, then loaded into a purely magnetic time-averaged orbiting potential (TOP) trap [10]. Atoms were further compressed by changing the TOP field parameters, and then evaporatively cooled [11] to condensation. The condensate and thermal cloud were imaged using absorptive and dark-ground [12] techniques.

Our approach deviated from prior work in the following respects. First, the bulk of the evaporation was done by reducing the strength of the rotating component of the TOP magnetic field, while maintaining a fixed quadrupole field gradient, rather than by radio-frequency (rf)-induced evaporation. Second, we carefully tailored the evaporation sequence through a piecewise optimization of evaporation parameters. This allowed us to obtain efficient evaporation with relatively small numbers of atoms. Third, we directly imaged the trap with an $f/2.5$ optical system through high-quality optical viewports. Finally, we achieved a performance enhancement during the MOT loading period by capturing atoms in a hybrid trap consisting of a MOT plus a weak rotating magnetic bias field.

An illustration of our apparatus is shown in Fig. 1. A Rb partial pressure was maintained in the main vacuum chamber with a Rb-coated cold finger. Antireflection-coated optical viewports, used to admit laser light, were attached to the

stainless-steel chamber with indium metal seals. The $10\text{ cm} \times 10\text{ cm} \times 2.5\text{ cm}$ main chamber was mounted between a pair of anti-Helmholtz coils oriented with their symmetry axis parallel to gravity. The coils were capable of producing a spherical quadrupole magnetic field with linear gradients of 300 G/cm (in the radial, or horizontal, direction) at full current. Four additional coils were used to create the rotating bias field of the TOP trap. The bias field rotated at a frequency of 10.5 kHz in the horizontal plane and could be varied in strength up to 36 G .

Atoms were initially collected from the background vapor into a MOT. Each of the MOT laser beams had a $1/e^2$ diameter of $\sim 1.2\text{ cm}$, an intensity of $\sim 10I_{sat}$, and was tuned 9 MHz to the red of the ^{87}Rb $5S_{1/2}$, $F=2$ to $5P_{3/2}$, $F'=3$ transition (I_{sat} is the saturation intensity for the $F=2$, $m_f=2$ to $F'=3$, $m'_f=3$ transition). Another laser beam of intensity I_{sat} , tuned $\sim 5\text{ MHz}$ below the $F=1$ to $F'=2$ transition, was used to repump atoms. A 4-mm-diam dark spot in the center of this beam, filled with a second beam tuned to the $F=2$ to $F'=2$ transition, was used to mitigate

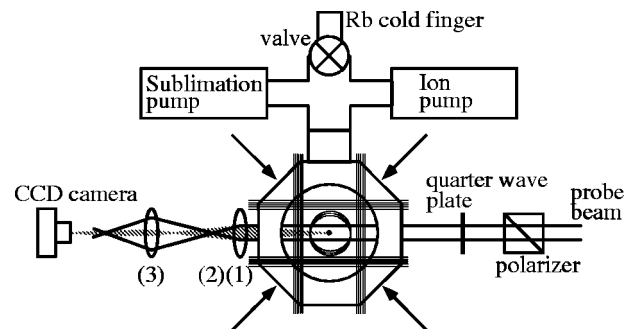


FIG. 1. Schematic view of the experimental apparatus, showing the vacuum chamber (octagon) and imaging optics (not to scale). The straight lines overlapping the octagon represent the TOP coils that surround the chamber, and the smaller circles represent the rf evaporation coils. The four dark arrows represent the four MOT beams that lie in the horizontal plane. The beam paths of the probe beam (dark lines) and the light diffracted and refracted by the atoms (shaded area) are also shown. The lens at position (1) collects the diffracted and refracted light, which is imaged onto the CCD by the lens at position (3). Position (2) indicates the focus of the unscattered probe light, which is the position of the dark-ground imaging beam block.

light-assisted, density-dependent collisional losses. These losses were further reduced by loading the MOT with a weak (~ 5 G) rotating field component (created using the TOP coils described above), in addition to a quadrupole field gradient of 5 G/cm, lowering the atomic density in the central region of the trap. Operating at a vapor-pressure-limited $1/e$ loading time constant of ~ 90 s, we typically loaded $\sim 10^8$ atoms in a ~ 150 -s interval.

Following this loading stage, atoms were compressed, then cooled, before being transferred into a purely magnetic trap. To compress atoms, the rotating bias field was turned off, the hole in the center of the repumping beam was filled with repumping light tuned to the $F=1$ to $F'=2$ transition, the trapping frequency was detuned to 42 MHz below resonance, and the strength of the spherical quadrupole field was ramped to ~ 8 G/cm. After this 100-ms compression stage, the quadrupole field was turned off and the atoms were cooled in optical molasses for 1 ms. The molasses beams were then extinguished, and the atoms were optically pumped into the $F=2$, $m_f=2$ Zeeman sublevel by turning on a ~ 7 G rotating bias field and subjecting the atoms to five resonant, circularly polarized, optical pulses of intensity $I=0.1I_{sat}$, each pulse having a 16- μ s duration. The pulses were synchronized with the rotation rate of the field, and occurred when the bias field direction was collinear with the propagation direction of the pumping beam.

The optically pumped atoms were then transferred into the TOP trap. At the end of the optical pumping cycle, the spherical quadrupole field was snapped onto a radial gradient of $B'_q=55$ G/cm, while the TOP field was simultaneously established at a strength of $B_{rot}=10$ G (500- μ s switching time for each field). The field strengths were then linearly ramped over a 900-ms interval to $B'_q=275$ G/cm and $B_{rot}=36$ G. The number of atoms in the magnetic trap at this point was $\sim 10^7$ and the phase-space density of the cloud was $\sim 2 \times 10^{-6}$ [13]. The parameters used for the transfer were optimized to maximize the phase-space density of the magnetically trapped atoms.

Atoms were compressed and evaporatively cooled after being loaded into the TOP trap by reducing the strength of the rotating field. For a TOP trap, the trap curvature is $\propto B_q'^2/B_{rot}$, so reduction in B_{rot} increases the trap curvature, and hence compresses atoms. The trap depth, on the other hand, scales as B_{rot} , and thus decreases with decreasing B_{rot} . The combination of these two effects enables efficient evaporative cooling by reducing B_{rot} , since the compression realized with reduction in trap depth enhances the two-particle collision rate and speeds up the ensemble thermalization rate.

The rotating TOP field strength was ramped down in multiple stages. The duration and change in B_{rot} for each segment of the TOP ramp were optimized for maximum phase-space density increase (Fig. 2). We measured phase-space density using standard absorptive imaging techniques, as described below. Over the course of the 24-s TOP-induced evaporation sequence, the loss in number of atoms was a factor of ~ 100 , while the phase-space density increased nearly six orders of magnitude to $\sim 10^{-1}$ [14].

The density and temperature of the trapped atoms were determined through absorptive imaging. Our imaging geom-

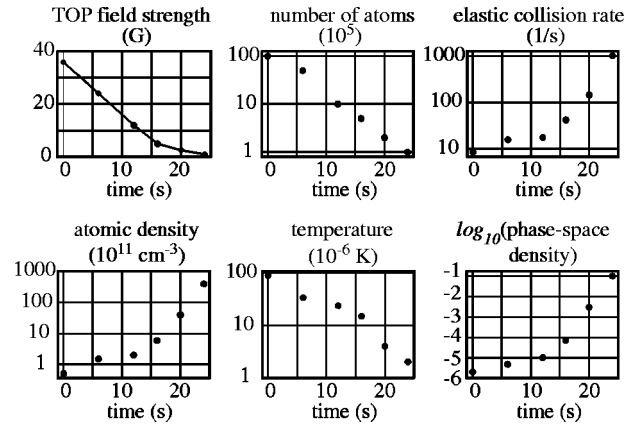


FIG. 2. Evaporation characteristics vs time for the TOP evaporative cooling ramp. The horizontal axes indicate the time of a measurement, referenced to the beginning of the TOP field evaporation ramp.

etry is illustrated in Fig. 1. Atoms were irradiated with up to four pulses of low-intensity ($\sim 10^{-3}I_{sat}$) light resonant (or nearly resonant) with the optical transition. Each 16- μ s, circularly polarized, pulse was flashed on synchronously with the TOP field when the TOP field direction was parallel with the probe propagation axis. The shadow cast by absorption from the atomic cloud was imaged onto a cooled charge-coupled-device (CCD) camera. The magnification of our imaging system was 7.0 ± 0.3 . The calculated diffraction-limited resolution was $\sim 2.6 \mu\text{m}$ ($1/e$ radius), while the measured resolution was $3.9 \pm 0.3 \mu\text{m}$. This measurement was made *in situ* by imaging small ensembles of atoms in tight trapping potentials, and independently by imaging test targets.

The intensity in the image plane is proportional to $1 - \exp[-\alpha(x,y)]$, where $\alpha(x,y) = \int n(\mathbf{r})\sigma dz$ is the optical depth of the atom cloud, $n(\mathbf{r})$ is the cloud density at position \mathbf{r} , and σ is the optical scattering cross section. We analyzed the images by first extracting $\alpha(x,y)$ from the images, then fitting $\alpha(x,y)$ to a Gaussian distribution. Cloud temperatures were extracted from the fitted widths of $\alpha(x,y)$, and densities inferred from optical depths and widths. The total atom number was obtained from the density and size measurements. For the highest phase-space densities, the trapping potential was first adiabatically relaxed to ensure that the peak optical depth was on the order of unity. The phase-space density in the unrelaxed potential was inferred by scaling from those obtained in the relaxed potentials [15].

The final stage of evaporative cooling was accomplished with rf magnetic fields, enabling precise control of the energy of this evaporative cut. The rf field was established using two coils mounted just outside the chamber against two windows. The rf frequency was linearly ramped down in a 2-s cooling interval. The final temperature depended on the rf frequency at the end of the ramp.

The threshold rf frequency for condensate formation depended on B_{rot} and the number of atoms in the trap, and was measured by changing the final frequency of the sweep [16]. In order to obtain reliable images of the condensate, B'_q was adiabatically relaxed following this rf sweep. This reduced the optical depth of the cloud and increased its size. We typically reduced the trap-spring constants by a factor of 10^3

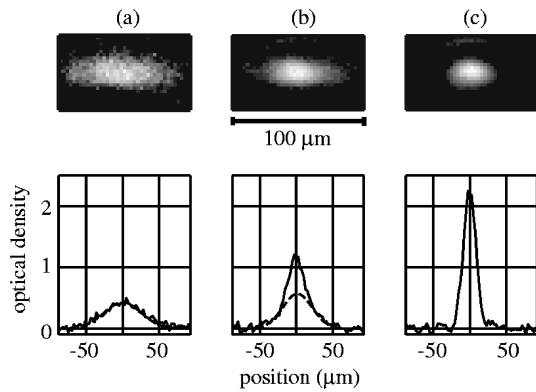


FIG. 3. Absorption images and corresponding optical-density cross sections showing the BEC phase transition. Three different final rf values of the rf evaporative cooling ramp are represented: (a) a frequency of 1.80 MHz, which was just above the condensation threshold; (b) 1.75 MHz, which was just below the threshold; and (c) 1.68 MHz, which was far enough below the threshold to produce a nearly pure condensate (normal fraction is not resolvable). In (a), a single Gaussian distribution fits the data well. For (b), the fit of a Gaussian distribution to the wings of the normal fraction is shown.

over a 0.4-s interval. The elastic collision rates were high enough that the condensate was expected to maintain thermodynamic equilibrium with the normal fraction over the duration of this expansion.

Figure 3 shows images above and below the condensation threshold. The images were analyzed by fitting two two-dimensional Gaussian distributions to $\alpha(x,y)$. These Gaussians fit a wide distribution, corresponding to the normal (uncondensed) fraction at the wings of the observed atom cloud, and a narrow distribution, corresponding to condensed atoms at the center of the atom cloud. We extracted the optical depth and size for both the normal and condensed fractions of the cloud from these fits. We then corrected the measured widths for the finite resolution of our imaging system. The temperature (T) was determined from the size of the normal cloud. The number of atoms in the condensate (N_0) and in the normal fraction were inferred from the optical depth and size of each component. The total number of atoms (N) was determined by summing the number in each component.

As an independent check on our imaging we also observed the transition using the dispersive dark-ground imaging technique [12]. In this case, the image forms as a result of the lensing of the light as it refracts on its passage through the atomic cloud. The image is observed by blocking the nonrefracted beam at its focus in the imaging system, as described in Ref. [17]. For this imaging technique, the optical intensity at the image plane is proportional to $\phi^2(x,y)$, where $\phi(x,y)$ is the dispersive phase shift for a ray that passes through the cloud at transverse position (x,y) . This expression is strictly valid for $\phi(x,y) \ll 1$ in the far-detuned limit. For the conditions of our images, the maximum values for ϕ approach 1 rad. We analyzed these images by fitting Gaussians to $\phi(x,y)$, then extracted temperature, number, and condensate fraction as described above.

For a noninteracting Bose gas in the thermodynamic limit ($N \rightarrow \infty$), the condensate fraction is $N_0/N = 1 - (T/T_0)^3$, with a transition temperature of $k_B T_0 = \hbar \bar{\omega} [N/\zeta(3)]^{1/3}$,

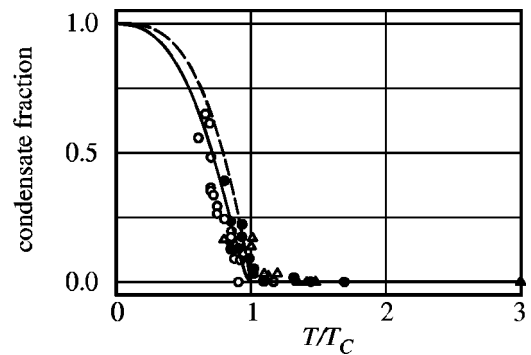


FIG. 4. Condensate fraction as a function of $T/T_0(N)$. The filled circles represent data taken with absorption imaging at a trap strength of $\omega_{\perp} = 2\pi \times 8$ rad/s, the open circles represent data taken with absorption imaging at a trap strength of $\omega_{\perp} = 2\pi \times 13$ rad/s, and the triangles represent data taken with dispersive dark-ground imaging at a trap strength of $\omega_{\perp} = 2\pi \times 13$ rad/s. Each data point represents a single image. The shot-to-shot variance of the total number N was approximately 30%. The solid curve is the expected behavior of the condensate fraction with the temperature in the semi-ideal gas limit (see Ref. [19]), and is not a fit to the data. The dashed curve illustrates the expected behavior of a noninteracting gas.

where $\bar{\omega}$ is the geometric mean of the trap oscillation frequencies [18]. A more refined theory that includes the effects of weak interactions is given in Ref. [19]. These theories are compared with our data in Fig. 4, which shows N_0/N vs T/T_0 for three data sets. The first and second sets were taken using absorptive imaging, while the third set was taken using the dark-ground imaging technique. The trap strength (as characterized by the radial oscillation frequency ω_{\perp}) was $\omega_{\perp} = 2\pi \times 8$ rad/s for the first set, and $\omega_{\perp} = 2\pi \times 13$ rad/s for the second and third sets [20]. In this analysis, N_0/N , T_0 , and T were extracted directly from the images [21]. In order to avoid potential systematic biases in the absorption data, we captured these images at several probe detunings (ranging from -50 MHz to -10 MHz).

We characterized the strength of the mean-field interaction [22] through direct observation of the size and shape of the condensate. In the Thomas-Fermi limit, where the condensate kinetic energy is small compared with the mean-field energy, the condensate aspect ratio is $8^{1/2}$ and the density profile is parabolic. For smaller numbers of atoms, where kinetic energy is no longer negligible, a variational solution of the nonlinear Schrödinger equation can be used to predict the size and shape of the condensed cloud. A simple variational ansatz for the ground state is a Gaussian wave function [22]. With this assumption, one finds that the aspect ratio varies continuously between that of a harmonic-oscillator ground state, $8^{1/4}$, and the Thomas-Fermi value of $8^{1/2}$ as the number of atoms increases. For the data shown in Fig. 3(c) the observed condensate aspect ratio is 2.3 ± 0.3 , significantly less than the Thomas-Fermi prediction of 2.82. The error is dominated by uncertainty in the resolution of the imaging system. With a measured value of $N_0 \sim 3 \pm 1 \times 10^4$ atoms and $\omega_{\perp} = 2\pi \times 13$ rad/s, the aspect ratio predicted by a variational calculation using a Gaussian trial function is 2.7, 17% larger than the observed value. The predicted radial size

of $7.8 \mu\text{m}$ is slightly less than our observed radial size of $9.2 \pm 0.6 \mu\text{m}$. Note that the observed shift in the aspect ratio between the condensed and normal cloud is an independent signature of condensation, analogous to the anisotropic momentum distributions observed in the initial Bose-Einstein condensation (BEC) studies. For comparison, the normal fraction aspect ratios of the images shown in Figs. 3(a) and 3(b) are ~ 2.8 . (The expected normal fraction aspect ratio, determined by the trap equipotential surfaces, is $8^{1/2}$.)

In conclusion, we have demonstrated Bose-Einstein condensation of ^{87}Rb and have shown that direct imaging techniques can be used to obtain quantitative comparisons with theory for relatively small numbers of atoms. We expect further study of finite systems to provide crucial insights into the role of quantum fluctuations in the formation of the condensate.

This work was supported by the NSF and the ONR.

-
- [1] M. Anderson *et al.*, *Science* **269**, 198 (1995).
 [2] C. Bradley *et al.*, *Phys. Rev. Lett.* **75**, 1687 (1995).
 [3] K. Davis *et al.*, *Phys. Rev. Lett.* **75**, 3969 (1995).
 [4] J. Ensher *et al.*, *Phys. Rev. Lett.* **77**, 4984 (1996).
 [5] M. Mewes *et al.*, *Phys. Rev. Lett.* **77**, 416 (1996).
 [6] E. Raab *et al.*, *Phys. Rev. Lett.* **59**, 2631 (1987).
 [7] W. Ketterle *et al.*, *Phys. Rev. Lett.* **70**, 2253 (1993).
 [8] M. Anderson *et al.*, *Phys. Rev. A* **50**, R3597 (1994).
 [9] W. Petrich *et al.*, *J. Opt. Soc. Am. B* **11**, 1332 (1994).
 [10] W. Petrich *et al.*, *Phys. Rev. Lett.* **74**, 3352 (1995).
 [11] N. Masuhara *et al.*, *Phys. Rev. Lett.* **61**, 935 (1988).
 [12] M. Andrews *et al.*, *Science* **273**, 84 (1996).
 [13] Phase-space density is $n\lambda_{th}^3$, where $\lambda_{th} = \sqrt{2\pi\hbar^2/mk_B T}$ is the thermal de Broglie wavelength, and n is the atomic density.
 [14] This corresponds to an overall efficiency [defined as $\ln(\text{phase-space density increase})/\ln(\text{number lost})$] of 2.8.
 [15] Adiabatic changes in the trap potential by a factor κ change the trap density by $\kappa^{3/4}$ and temperature by $\kappa^{1/2}$, for a harmonic three-dimensional trapping potential. See W. Ketterle and N. van Druten, *Phys. Rev. A* **37**, 181 (1996).
 [16] We were also able to achieve condensation solely through manipulation of the TOP field strength, without the use of an rf cooling ramp. However, this method was not as efficient as the hybrid sequence described in the text.
 [17] See, for example, J. Goodman, *Introduction to Fourier Optics* (Mc-Graw Hill, New York, 1968).
 [18] S. R. de Groot *et al.*, *Proc. R. Soc. London, Ser. A* **203**, 266 (1950).
 [19] M. Naraschewski and D. Stamper-Kurn, *Phys. Rev. A* **58**, 2423 (1998).
 [20] These frequencies were inferred from the measured magnetic-field strengths.
 [21] To determine the dependence of N (and thus T_0) on T for the data of Fig. 4, we first fit a line to N vs T data extracted directly from our images and then used the fitted functional form to compute the normalized condensate temperature T/T_0 . This suppressed the $\sim 10\%$ shot-to-shot variance in the normalizing parameter T_0 .
 [22] See, for example, G. Baym and C. Pethick, *Phys. Rev. Lett.* **76**, 6 (1996).